

The Effect of Halide Composition on the Luminescent Properties of Ternary Cesium–Copper Halide Pseudo-Perovskite Films

Gergely Ferenc Samu,* Tamás Sándor Zsigmond, Cintia Hajdu, Mátyás Hunyadi, Lóránt Csige, Attila Csík, Judit Kopniczky, Béla Hopp, and Csaba Janáky*


Ternary copper halide pseudo-perovskites are in the forefront of research as potential active materials in light emission applications. The optoelectronic properties of these compounds can be fine-tuned by the preparation of mixed-halide compositions. After irradiation, self-trapped excitonic states are formed in these materials. However, the emission from these self-trapped states is not yet fully understood. In this work, mixed-halide $\text{Cs}_3\text{Cu}_2\text{X}_5$ films (where X: I and/or Br) are prepared by a simple spray-coating method. Using ultraviolet photoelectron spectroscopy, the changes in optoelectronic properties are linked to the electronic structure of these materials. It is revealed that the incorporation of bromide into the lattice makes the emission process of these materials more vulnerable to trap states. By combining the different spectroscopic characterization techniques, the exact band structure of these compounds is determined, and the different processes are translated to the absolute energy scale. As an alternative excitation mechanism of self-trapped states, α -particles are used to induce radioluminescence response. The $\text{Cs}_3\text{Cu}_2\text{X}_5$ films exhibit composite decay patterns, most likely attributed to a multitude of different trap state-mediated recombination processes.

1. Introduction

Ternary copper halide (TCH) pseudo-perovskites are a rapidly emerging class of materials in the field of optoelectronics.^[1,2] Their crystal structure differ from conventional perovskites (Scheme 1A) as the copper(I) with large halide ions (e.g., Br^- and I^-) lacks the characteristic octahedral units. Instead $[\text{Cu}_2\text{X}_5]^{2-}$ motifs are formed, consisting of a Cu centered tetrahedron with four halogen atoms, and another equilateral triangle, where a further Cu is located at the center position. This 0D structure (Scheme 1B) bestows these materials with unique light emission properties. These perovskite-derived compounds offer to remedy some of the shortcomings of their lead-halide predecessors, such as: i) ambient instability, ii) toxicity of Pb, iii) thermal instability, and iv) parasitic self-absorption of emitted light.^[3] Thanks to their composition-tunable optoelectronic properties, the hallmark of perovskite materials, TCHs are mostly explored as effective light emitters.^[4] Their utilization in lighting applications (blue^[5] and white LEDs),^[6] solar concentrators,^[7,8] radiation detectors^[9–13] and scintillation detectors,^[14] nuclear batteries,^[15] anticounterfeiting applications,^[16,17] and UV light-detection^[18] has sparked significant attention.

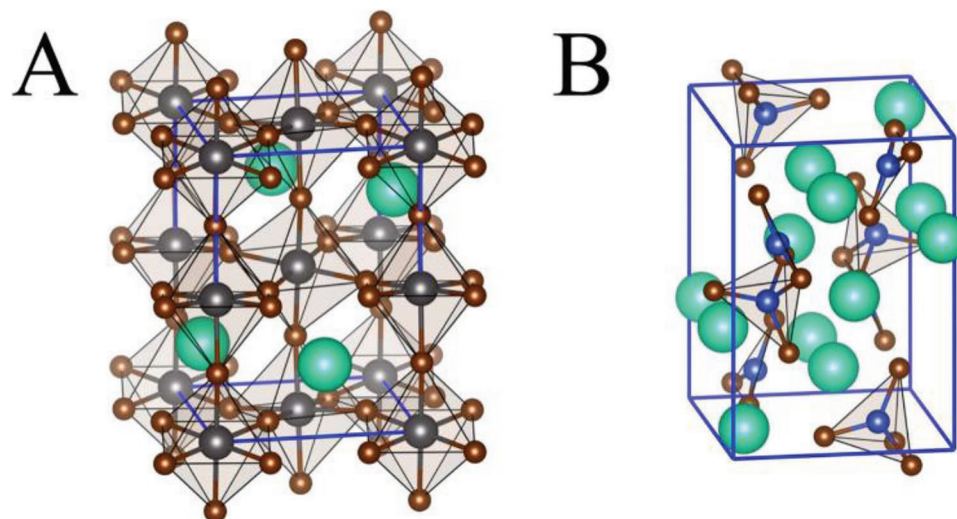
The light emission process in TCH compounds involves self-trapped excitonic states (STEs) that are formed through lattice distortions after excitation.^[19,20] These are the result of strong phonon–electron coupling and the soft crystal lattice of these materials.^[7] In stark contrast to defect state emissions, these are difficult to saturate as revealed by intensity dependent photoluminescence (PL) measurements.^[19,21] After photoexcitation of TCHs, free carriers are generated that quickly form excitons.^[4] This is followed by the rapid trapping of excitons into these STE states, which process occurs on the sub-ps timescale.^[22] Multiple excitonic states are proposed to exist in these materials.^[20] These, however, can only be observed under low temperature conditions^[19,23] and not at room temperature.^[24] Light emission from these STE states is spectrally wide, significantly Stokes-shifted and possesses a long PL lifetime (generally in the microsecond time range). At the same time, the emission process

G. F. Samu, T. S. Zsigmond, C. Hajdu, C. Janáky
Department of Physical Chemistry and Materials Science
Interdisciplinary Excellence Centre
University of Szeged
Aradi V. tere 1, Szeged H-6720, Hungary
E-mail: samugf@chem.u-szeged.hu; janaky@chem.u-szeged.hu
M. Hunyadi, L. Csige, A. Csík
Institute for Nuclear Research
Bem tér 18/c, Debrecen H-4026, Hungary
J. Kopniczky, B. Hopp
Department of Optics and Quantum Electronics
University of Szeged
Dóm tér 9, Szeged H-6720, Hungary

 The ORCID identification number(s) for the author(s) of this article can be found under <https://doi.org/10.1002/adom.202300825>

© 2023 The Authors. Advanced Optical Materials published by Wiley-VCH GmbH. This is an open access article under the terms of the Creative Commons Attribution-NonCommercial License, which permits use, distribution and reproduction in any medium, provided the original work is properly cited and is not used for commercial purposes.

DOI: 10.1002/adom.202300825



Scheme 1. Depiction of the crystal structure of A) the conventional perovskite material CsPbBr₃ (COD #4510745) and B) the pseudo-perovskite material Cs₃Cu₂Br₅ (COD #7246299). The blue lines represent the unit-cell.

seems to be unaffected by defect states within these materials and is protected by a large detrapping barrier, which results in high quantum yields.^[25]

The main TCH compositions generally explored are Cs₃Cu₂X₅ and CsCu₂X₃ (where X: Cl, Br, or I). The 0D structure of Cs₃Cu₂X₅ further enhances the self-trapping process resulting in higher quantum yields, compared to its 1D CsCu₂X₃ counterpart.^[22] The valence band (VB) of TCH compounds is mainly composed of the hybridized 3*d* orbitals of Cu and the *np* orbitals of the respective halide component.^[1] In a similar fashion, the conduction band (CB) has contributions from the 4*s* orbitals of Cu and the halide *np* orbitals. Theoretical calculations show that the Cs in the lattice has no effect on the band structure.^[26,27] The halide composition of the films therefore, will inevitably affect the band structure and the respective density of states (DOS) of these materials. Importantly, after photoexcitation, the excited state is formed after lattice distortions, which will also affect the band structure.^[7]

The preparation of mixed-halide variants of hybrid lead-halide perovskites is an attractive approach to fine tune their optoelectronic properties.^[28] This halide interchangeability also exists in TCH materials. In the case of Cs₃Cu₂X₅, the gradual exchange of the halide from I to Br induces a slight red-shift in the PL wavelength maximum (from 444 to 456 nm)^[27,29] and also increases the PL lifetime notably (from 1 μs in the case of I, to 22 μs in the case of Br).^[30] The effect of the bromide content on the quantum yield (QY) of mixed-halide variants is more convoluted, as the determined QY values for mixed compositions always lies closer to the values of pure Cs₃Cu₂Br₅ samples.^[27,31] This can be rooted in the different ambient stability of TCH compounds (e.g., moisture, oxygen, and temperature) as Cs₃Cu₂I₅ remains stable under months of storage, while the surface of Cs₃Cu₂Br₅ can undergo moisture-induced oxidation.^[31] The preparation of mixed compositions of Cs₃Cu₂Br_{*x*}I_{5-*x*} can be achieved by different synthesis strategies, such as: mechanochemical methods,^[31] high-temperature solid state synthesis,^[27] rapid cooling crystallization method,^[32] or antisolvent recrystallization method.^[30] The soft

lattice of these compounds also allows post-synthetic modification of the parent Cs₃Cu₂X₅ structure, resulting in only structural change^[17] or complete halide exchange.^[16,33] In most cases, film preparation from mixed-halide layers is performed by pre-synthesis of the powders or nanocrystals, which is followed by a layer formation step.^[29] Immediate film formation strategies, such as single-source vacuum deposition^[31] or spray coating^[14] have been rarely used.

In this work, we prepared mixed-halide Cs₃Cu₂X₅ films (where X: Br and/or I) with precisely controlled composition, via a simple spray coating technique. We studied the effect of halide-composition on the optoelectronic properties of the materials. Using ultraviolet photoelectron spectroscopy (UPS), we link the changes in optoelectronic properties to the alteration of the electronic structure. Using the information gathered from the different spectroscopic techniques, we experimentally determined the detailed band diagram of these materials. We also aimed to reveal whether the change in the PL properties of the layers is directly reflected in the radioluminescence (RL) response following their exposure to α-particles from a radioactive source.

2. Results and Discussion

The thickness of the prepared layers was evaluated by profilometry (Figures S1 and S2, Supporting Information) as detailed in the Experimental Section. In all cases good agreement with the 10 μm nominal thickness was found, and similar surface roughness was achieved (Table S1, Supporting Information) which signals that the precursor solution composition has negligible effect on the layer formation process. To reveal whether the desired mixed-halide Cs₃Cu₂I_{*x*}Br_{5-*x*} layers were formed, we carried out XRD measurements (Figure 1A; Figure S3A–F, Supporting Information). Le Bail fitting of the obtained diffraction patterns to a *Pnma* structure revealed phase pure composition for almost all compositions except Cs₃CuBr₅ and Cs₃Cu₂Br_{2.5}I_{2.5} (as shown in the Figure S3, Supporting Information). In these cases, one

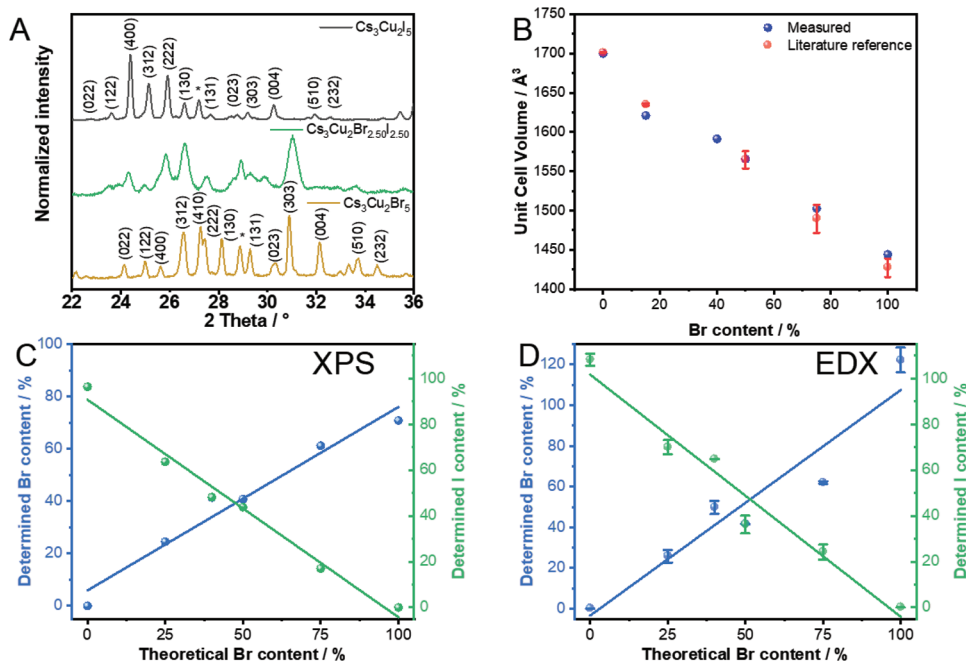
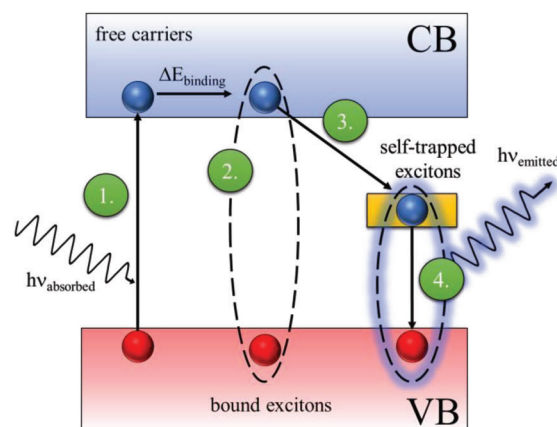


Figure 1. A) XRD patterns of $\text{Cs}_3\text{Cu}_2\text{I}_5$, $\text{Cs}_3\text{Cu}_2\text{Br}_{2.50}\text{I}_{2.50}$, and $\text{Cs}_3\text{Cu}_2\text{Br}_5$ layers. B) The effect of bromide incorporation on the unit cell volume of $\text{Cs}_3\text{Cu}_2\text{I}_x\text{Br}_{5-x}$ materials, determined from the XRD patterns and compared with values obtained from literature, where the error bars represent dispersion in the reported values for mixed compositions.^[27,31] C) Surface composition determined from XPS analysis. D) Bulk composition determined from EDX measurements. The error bars in the case of EDX measurements represent measurements for three different layers.

additional reflection (marked with an asterisk) was found in both samples, presumably from a small amount of Cs-halide impurity. Shifted reflections were observed in the case of the mixed-halide layers, compared to the single halide containing counterparts, within the boundaries set by the single-halide compositions. From the Le Bail fitting we determined the unit cell parameters (Figure S4A–C, Supporting Information) and the unit cell volume (Figure 1B). By increasing the bromide content, a gradual contraction of the unit cell was observed (as depicted in Figure S5, Supporting Information). This is in good agreement with the difference in ionic radius between the halides and signals the incorporation of bromide into the pseudo-perovskite lattice. All unit cell parameters show similar dependence on the bromide content of the samples, which reveals that there is no preferential direction for bromide incorporation. The determined unit cell parameters and volume are in good agreement with literature values.^[27,31] A broadening of the reflections was also observed for the mixed samples (compared to the single halide containing materials). This was the largest for intermediate compositions, which could signal i) a decrease in the crystallite domain size or ii) the increase in the crystallographic strain for these compositions. Top-down SEM images of the $\text{Cs}_3\text{Cu}_2\text{I}_x\text{Br}_{5-x}$ layers showed a granular morphology for all prepared compositions (Figure S6, Supporting Information). The spray coating process resulted in films with full coverage of the substrates and grain sizes on the order of several microns. The surface and bulk composition of the $\text{Cs}_3\text{Cu}_2\text{I}_x\text{Br}_{5-x}$ layers was determined by XPS (Figure 1C) and EDX measurements (Figure 1D), respectively. Detailed discussion on the evaluation of the XPS spectra can be found in the Supporting Information (Figure S7 and Tables S2–S4). Quantification of the surface halide content of the $\text{Cs}_3\text{Cu}_2\text{I}_x\text{Br}_{5-x}$ layers

revealed slight bromide deficiency of the higher bromide containing layers compared to the EDX measurements (Table S5, Supporting Information). This could signal the possible formation of trap states on the surface of these compositions, as elaborated in what follows.

Steady-state PL and UV–vis absorption measurements were carried out to reveal the effect of the bromide content on the optoelectronic properties of the $\text{Cs}_3\text{Cu}_2\text{I}_x\text{Br}_{5-x}$ layers. We aimed to characterize the different electronic transitions as depicted in Scheme 2 and tie the various processes to exact energy levels. UV–vis spectroscopy measurements can be used to reveal the lowest energy transition (bandgap) between the VB and CB edges in these materials (Scheme 2 – 1st process). Recording PL excitation spectrum can also be used to determine the bandgap of an emitting material. In these experiments the excitation wavelength is scanned, while the detection is carried out at the characteristic wavelength of PL emission of the samples. In these materials, however, the PL emission is directly linked to the appearance of the STE state (Scheme 2 – 4th process). To induce the necessary lattice distortions to form these STE states, bound excitons must be formed first (Scheme 2 – 2nd process). The bandgap energy determined from PL excitation spectra (apparent E_{BG}) will contain this exciton binding energy as the relaxation of free carriers in TCH materials is non-radiative. The formation of the STE state by the bound exciton requires energy to induce the lattice distortions (Scheme 2 – 3rd process). This self-trapping energy will shift the PL emission to lower wavelengths and induce a large Stokes-shift in these materials. To place these transitions on the absolute energy scale we determined the VB positions from UPS measurements and coupled them with these optical characterization techniques.



1. Light absorption induced free carrier formation (determined from UV-vis onset)

$$h\nu_{\text{absorbed}} \geq E_{\text{BG}}$$

2. Exciton formation (difference between E_{BG} from PL excitation spectra and UV-vis onset)

$$\text{Apparent } E_{\text{BG}} = E_{\text{BG}} + \Delta E_{\text{binding}}$$

3. Self-trapping energy (difference between E_{BG} from UV-vis onset and STE emission energy)

$$E_{\text{ST}} = E_{\text{BG}} - E_{\text{PL}}$$

4. STE emission (PL peak position)

$$E_{\text{PL}} = h\nu_{\text{emitted}}$$

Scheme 2. Electronic transitions within materials with STE energy levels. Description of the different processes together with the used measurement technique for its determination.

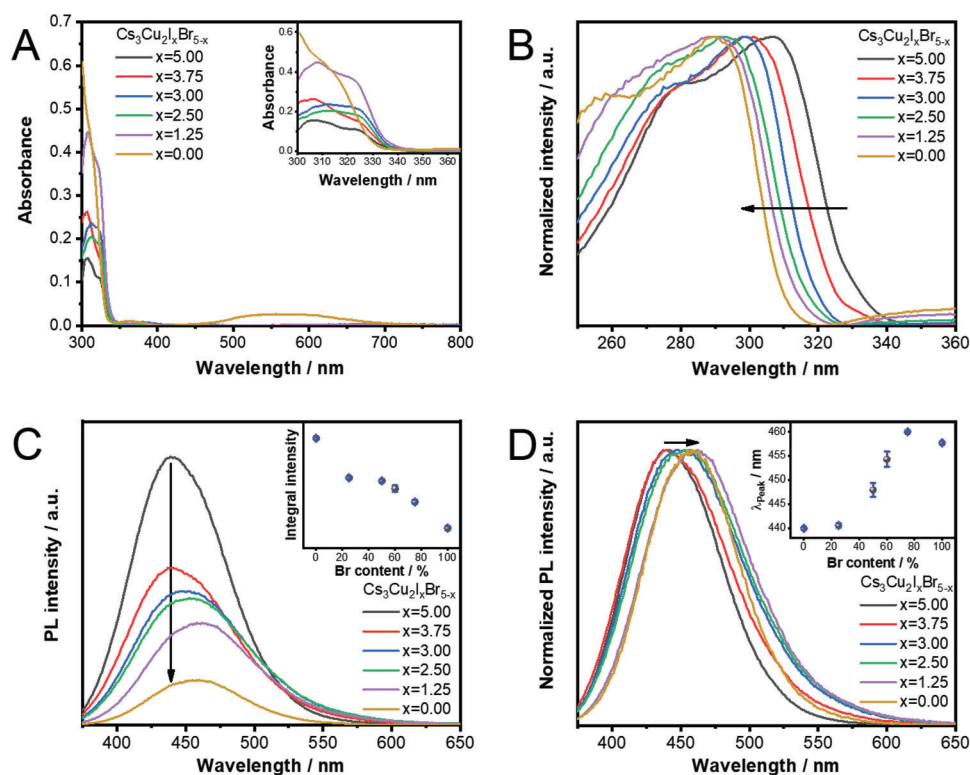


Figure 2. A) UV-vis spectra of $\text{Cs}_3\text{Cu}_2\text{I}_x\text{Br}_{5-x}$ layers recorded in transmission mode. Inset shows the magnified band-edge region. B) Normalized excitation spectra of $\text{Cs}_3\text{Cu}_2\text{I}_x\text{Br}_{5-x}$ layers, recorded at their respective PL maximum. C) Steady state PL spectra of $\text{Cs}_3\text{Cu}_2\text{I}_x\text{Br}_{5-x}$ layers. Inset shows the composition dependence of the integral intensity of the PL spectra. D) Normalized steady state PL spectra of $\text{Cs}_3\text{Cu}_2\text{I}_x\text{Br}_{5-x}$ layers. The inset shows the change in PL emission maximum with the composition. The emission maximum was determined from the first derivative of the recorded PL spectra. The excitation wavelength was 300 nm in all PL related measurements. The error bars in the insets represent first derivative measurement for three different layers.

We carried out UV-vis spectroscopy measurements to determine the bandgap of the prepared $\text{Cs}_3\text{Cu}_2\text{I}_x\text{Br}_{5-x}$ layers (Figure 2A). All films absorb light in the UV region and have only negligible light absorption in the visible range. Only $\text{Cs}_3\text{Cu}_2\text{Br}_5$ samples showed a broad absorption band between 500–650 nm which might originate from small quantities of formed Cu(II) within the layers in the form of $[\text{CuBr}_4]^{2-}$. To determine the

energy required to form the STE state for each composition PL excitation spectra of the $\text{Cs}_3\text{Cu}_2\text{I}_x\text{Br}_{5-x}$ layers were recorded (Figure 2B). It is apparent that with increasing bromide content, the blue-shift of the excitation spectra onset can be observed. This signals that the bromide content of the samples has a marked influence on the exciton binding energy of the compounds. To gain information on the energy position of the STE emission with

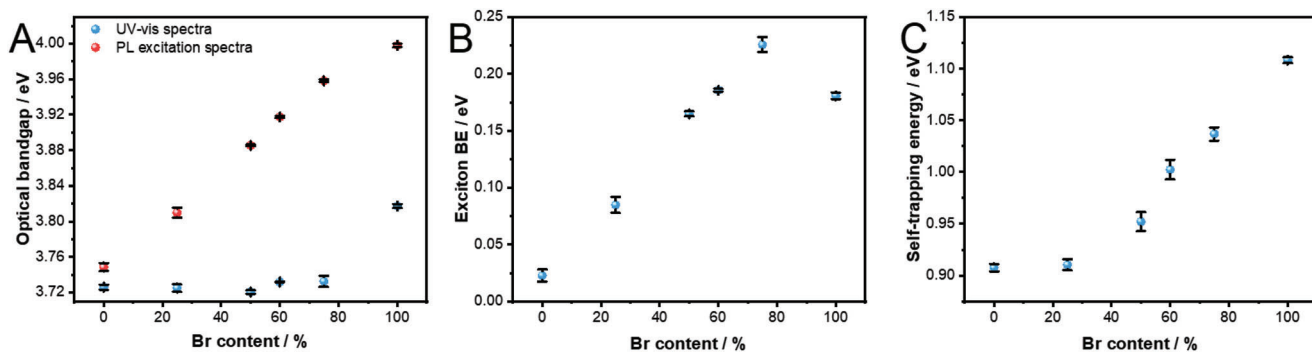


Figure 3. A) The composition dependence of the determined bandgap values for the $\text{Cs}_3\text{Cu}_2\text{I}_x\text{Br}_{5-x}$ layers, from the different optical techniques employed in this study. B) The change in the exciton binding energy and the C) variation of the self-trapping energy with the layer composition.

respect to the VB edge, we recorded the steady-state PL spectra of the mixed-halide layers (Figure 2C,D). The most prominent effect of the increasing bromide content is the gradual decrease of the PL intensity (Figure 2C), compared to the $\text{Cs}_3\text{Cu}_2\text{I}_5$ layers. This is also reflected in the absolute internal quantum yield (PLQY) of the layers (Figure S8, Supporting Information). The PLQY steadily decreases from 71% measured for $\text{Cs}_3\text{Cu}_2\text{I}_5$ layers to only 10% for $\text{Cs}_3\text{Cu}_2\text{Br}_5$ layers. Interestingly, this trend is foreshadowed in the literature, as the $\text{Cs}_3\text{Cu}_2\text{Br}_5$ samples often show low quantum yields (even compared to $\text{Cs}_3\text{Cu}_2\text{Cl}_5$) irrespective of the form of the samples (powders,^[34] quantum dots).^[30] This points toward the notion that the STE emission of $\text{Cs}_3\text{Cu}_2\text{Br}_5$ materials might be vulnerable to trap states (as opposed to its $\text{Cs}_3\text{Cu}_2\text{I}_5$ counterpart) as recombination through trap states is a non-radiative process that decreases the PLQY. The prepared $\text{Cs}_3\text{Cu}_2\text{Br}_5$ layers also suffer from the presence of the Cu(II) moiety in the film, as it i) can reabsorb portion of the emitted light and ii) act as a recombination center as it is located within the bandgap, further lowering the PLQY compared to the mixed bromide/iodide samples. The increasing bromide content also shifted the PL peak position of the layers to higher wavelengths, without altering the shape of the PL spectra (Figure 2D). This signals that no emissive secondary phases are formed during the preparation procedure, as that would distort the shape of the PL spectra. The PL peak position was used to determine the self-trapping energy.

The optical bandgap values determined from the UV-vis spectra and PL excitation spectra are summarized in Figure 3A. It is apparent that the increasing bromide content of the samples has negligible effect on the lowest energy transition (related to the bandgap) of the samples. In stark contrast, the bromide content of the layers had a strong impact on the required energy to induce the STE emission. The energy difference between the values obtained in these two measurements gives the exciton binding energy (Figure 3B). The increase in the bromide content increased the required energy to bind excitons within these materials. Similarly, the self-trapping energy (Figure 3C) is also larger in bromide rich compositions. This signals that it is energetically more difficult to induce lattice distortions in the bromide-rich materials, as bromide forms stronger bonds within the lattice. Furthermore, the formed self-trapped state lies deeper in the bandgap in the case of bromide-rich compositions.

The incorporated bromide also has a pronounced effect on the PL decay of the samples (Figure 4A,B). The $\text{Cs}_3\text{Cu}_2\text{I}_5$ layer showed a monoexponential decay with a 1.0 μs lifetime, which agrees well with literature values.^[12] With the incorporation of bromide into the pseudo-perovskite lattice, a new component (with a shorter lifetime) is observed (Table S6, Supporting Information). The shorter lifetime component becomes even shorter in the case of samples with high bromide content (Figure 4C). These also display the worst PLQY among all compositions. This shorter lifetime component might be related to the presence of surface trap states, which facilitate non-radiative recombination. In parallel, the longer lifetime component, which is related to the STE recombination process, increases with the increasing amount of incorporated bromide (Figure 4D). This longer lifetime component for the pure $\text{Cs}_3\text{Cu}_2\text{Br}_5$ sample falls short compared to the 18–30 μs lifetime typically observed in the literature.^[21,35]

To position the obtained optoelectronic data on the absolute energy scale, we performed UPS measurements on the $\text{Cs}_3\text{Cu}_2\text{I}_x\text{Br}_{5-x}$ layers. The calibration of the instrument and subtraction of the He(I) satellite lines were performed with a polycrystalline Ag foil (Figure S9, Supporting Information), as detailed in the Supporting Information. The UPS spectra (Figure S10A, Supporting Information) consisted of a sharp rise (secondary electron edge) which is followed by the features related to electron density in the VB of the materials. The second derivative of the UPS spectra (Figure S10B, Supporting Information) was used to determine the exact position of the secondary edge, which was used in the calculation of the work function of the materials (Figure S10C, Supporting Information). The work function showed a decrease with the incorporation of the bromide into the lattice, which translates to an increase in the Fermi-level. This signals that there is more electron density within the bandgap of bromide rich compositions. Closer inspection of the electron density around the VB edge also revealed the presence of these filled trap states. Background corrected UPS spectra of all $\text{Cs}_3\text{Cu}_2\text{I}_x\text{Br}_{5-x}$ compositions are summarized in Figures S11 and S12 (Supporting Information).

As the VB of these compounds consist of multiple hybrid orbitals, apparent semi-quantitative fits to the UPS spectra with five components were performed, in this manner the DOS are not linked to any specific hybrid orbital. The first four components

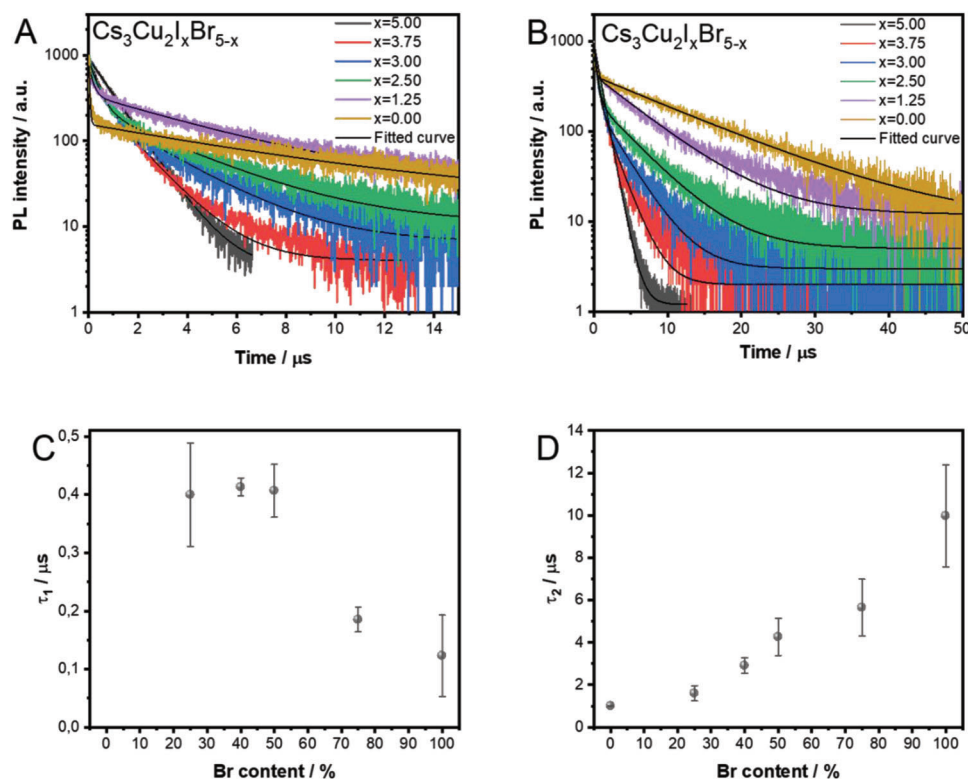


Figure 4. Composition dependence of the PL lifetime for the $\text{Cs}_3\text{Cu}_2\text{I}_x\text{Br}_{5-x}$ layers, recorded at the respective PL maximum for each sample, with a 320 nm LED light source excitation A) on a short and B) on a longer timescale. Effect of the composition on the C) short and D) long lifetime component of the PL decay. The error bars in the insets represent measurement for three different layers.

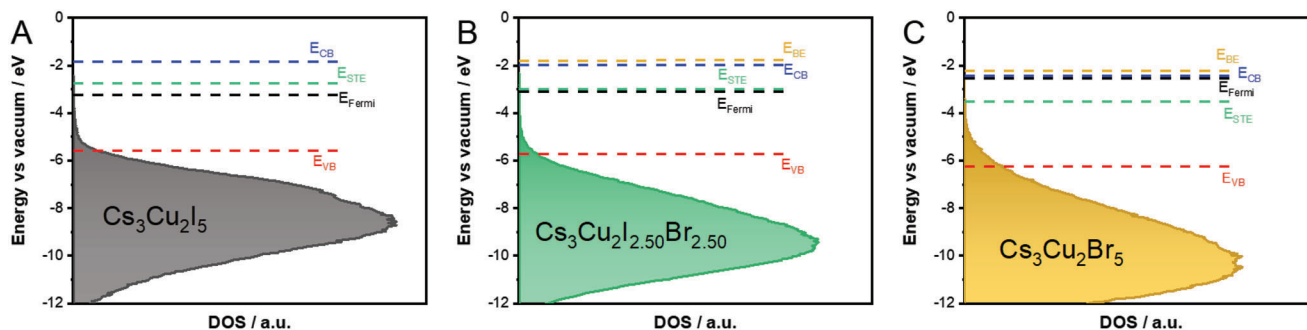


Figure 5. Band diagrams determined from the optical and UPS measurements for A) $\text{Cs}_3\text{Cu}_2\text{I}_5$, B) $\text{Cs}_3\text{Cu}_2\text{I}_{2.5}\text{Br}_{2.5}$, and C) $\text{Cs}_3\text{Cu}_2\text{Br}_5$ layers, respectively.

model the hybridized $3d$ orbitals of Cu and the np orbitals of the respective halides, while the fifth component is related to electron density within the bandgap (e.g., at trap states). The used fitting parameters are summarized in Table S7 (Supporting Information). Qualitatively, the increase in the bromide content of the films shifts the majority of the electron population within the VB to higher binding energies, further away from the Fermi level. Furthermore, in the case of bromide rich compositions, the contribution of the fifth component (trap state) also increases (Figure S12, Supporting Information). These changes can be directly linked to the inferior PL performance of the bromide rich compositions, as non-radiative recombination through these trap states can decrease the PLQY.

The VB positions determined from the UPS measurements (Figures S11 and S12, Supporting Information) were used, together with the calculated optoelectronic properties (bandgap, exciton binding energy, self-trapping energy in Figure 3), to visualize the detailed band structure of the $\text{Cs}_3\text{Cu}_2\text{I}_x\text{Br}_{5-x}$ layers (Figure 5). The increase in the bromide content shifts the VB maximum, and the majority of the electron population, to more negative energy values. Simultaneously, trap states within the bandgap appear with increasing population, which will in turn raise the Fermi-level of the samples with bromide-rich compositions to more positive values. In this manner, the Fermi-level overtakes the position of the STE energy level, which in turn might facilitate transfer of electrons from the trap-states to the

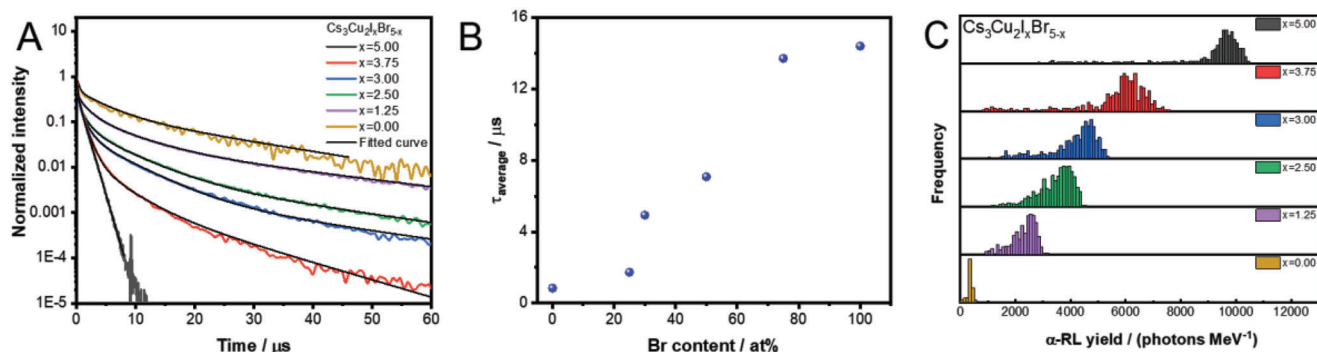


Figure 6. A) Event-averaged RL waveforms of the $\text{Cs}_3\text{Cu}_2\text{I}_x\text{Br}_{5-x}$ layers measured with 4.1 MeV α particles. The waveforms are normalized at their maximal amplitudes. B) Intensity-averaged RL lifetimes. C) Light-yield spectra shown with the same color coding of panel A.

STE states, detrimentally influencing the quantum yield of the bromide rich compounds.

The effect of bromide content on the luminescence properties of the $\text{Cs}_3\text{Cu}_2\text{I}_x\text{Br}_{5-x}$ layers has also been investigated with an alternative excitation method of the STE states, using α -particle exposure. The high excitation density due to the energy loss mechanism of α particles leads to the generation of hot charge carriers in a limited volume along the particle track, which can then populate a multitude of excitonic and trap states. These states with different potential-well parameters have different recombination characteristics, which can be observed as competing decay channels with varying decay time and amplitude in the RL response (Figure S13A, Supporting Information). The RL decay, recorded as event-averaged waveforms (Figure 6A; Figure S13B, Supporting Information), shows a similar trend as a function of the bromide ratio to one observed in the PL measurements. The multiexponential decomposition of the decay curves, however, looks apparently different, which indicates the sensitivity of recombination processes to the initial stages of the STE generation. The decay times for the various compositions are deduced by averaging the identified exponential components, using the corresponding light-yield intensities as weighting factors (Figure 6B). The extracted fitting parameters for the individual exponential components are summarized in Table S8 (Supporting Information). The total light yield of RL waveforms also shows a monotonous trend as a function of the bromide ratio. The histograms of total light yields are shown in Figure 6C. It is clearly seen that the increasing amount of bromide drastically suppresses the light yield accompanied with increasing decay times consistently with the results of PL data.

3. Conclusion

We successfully prepared different mixed-halide $\text{Cs}_3\text{Cu}_2\text{I}_x\text{Br}_{5-x}$ thin films with a simple spray-coating method, by altering the precursor solution composition. We have shown with different materials characterization techniques that the added bromide was incorporated into the pseudo-perovskite lattice. We thoroughly studied the effect of halide composition on the optoelectronic properties of the prepared thin films. With increasing bromide content, the gradual decrease of the PLQY was observed. This was coupled with the increase in the PL lifetime of the bromide rich $\text{Cs}_3\text{Cu}_2\text{I}_x\text{Br}_{5-x}$ compositions, with the simultaneous

evolution of a fast lifetime component. We attributed the fast lifetime component and the diminishing PLQY to the presence of bromide induced surface trap states within these compounds. As a further step to position these processes on the absolute energy scale, we performed UPS measurements. Together with the optoelectronic results, we determined the detailed band diagram of the compounds and revealed the position and density of trap states within their bandgap. We also performed luminescence measurements with an alternative excitation method of bright excitonic states using α -particle exposure. The increase of bromide content resulted in similar trends of light yields and decay properties as observed in the PL measurements supporting the outlined reordering of electronic states in the bromide-rich compositions.

4. Experimental Section

Materials: Cesium(I) iodide (CsI, Alfa Aesar, 99.9% trace metals basis), Cesium(I) bromide (CsBr, Merck, 99.999% trace metals basis), Copper(I) iodide (CuI, Alfa Aesar, Puratronic, 99.998% trace metals basis), Copper(I) bromide (CuBr, Merck, 99.999% trace metals basis), acetonitrile (ACN, VWR, 100%), and deionized (DI) water, were used for the preparation of the precursor solutions without further purification. The FTO (fluoride doped tin oxide, Merck, $\approx 7\ \Omega\ \text{cm}^{-2}$) covered glass substrates were cleaned with acetone (VWR, 100%), 2-propanol (VWR, 100%), and deionized (DI) water.

Preparation of the $\text{Cs}_3\text{Cu}_2\text{I}_x\text{Br}_{5-x}$ Solutions: The solutions (0.025 M) were prepared for the $\text{Cs}_3\text{Cu}_2\text{I}_x\text{Br}_{5-x}$ compounds in an acetonitrile/water mixture dissolving CsI, CuI, CsBr, and CuBr in the required stoichiometry. To ensure complete dissolution of the used precursors, water was added to the pure acetonitrile solvent. For low bromide containing variants ($x \geq 2.5$) 3.0 M, for $\text{Cs}_3\text{Cu}_2\text{I}_{1.25}\text{Br}_{3.75}$ 4.3 M, and for $\text{Cs}_3\text{Cu}_2\text{Br}_{5.0}$ 6.0 M water content was used.

Preparation of the $\text{Cs}_3\text{Cu}_2\text{I}_x\text{Br}_{5-x}$ Layers: The substrates (FTO coated glass or glass) were sonicated for 5 min in acetone, 2-propanol, and DI water before use. Immediately before spray coating, the substrates were subjected to 10 min of oxygen plasma treatment as well. The spray coating was performed with compressed air, with a $100\ \text{cm}^3\ \text{min}^{-1}$ airflow on the preheated substrates at $50\ ^\circ\text{C}$. Care was exercised between successive spray-coating cycles to ensure the evaporation of the solution from the substrate surface. By changing the number of spray coating cycles, a steady mass gain of the substrates could be observed, which translated to an increase in layer thickness (as seen for $\text{Cs}_3\text{Cu}_2\text{I}_5$ composition in Figure S1, Supporting Information). For materials characterization studies, layers with $\approx 10\ \mu\text{m}$ thickness were prepared from each composition. To determine the actual layer thickness of the samples and the quality of the formed layers profilometry measurements were performed for the

different mixed-halide compositions (Figure S2, Supporting Information). In the case of XPS and UPS studies 1 μm thick films were prepared to prevent charging of the layers. This thickness offered homogeneous coverage (no sign of Sn signal on the XPS spectra from the FTO substrate), while showed no charging of the layers.

Materials Characterization: A Veeco Dektak 8 contact-based profilometer was used to perform profilometry measurements on the thin films. A stylus with 2.5 μm radius was used applying a stylus pressure of 30 μN . UV-vis spectra of the layers in both transmission and diffuse reflection modes were recorded with a Shimadzu UV-3600 Plus instrument. Steady-state and time-resolved photoluminescence spectra were recorded with a Horiba FluoroMax spectrofluorimeter, equipped with a DeltaHub TC-SPC controller and a NanoLED-295 light source ($\lambda_{\text{max}} = 300 \text{ nm}$). Top-down scanning electron microscopy (SEM) images were captured with a Thermo Scientific Apreo 2 SEM instrument. X-ray diffraction (XRD) measurements were performed with a Rigaku MiniFlex 2 instrument with a $\text{Cu K}\alpha$ ($\lambda = 1.5418 \text{ \AA}$) X-ray source operated at 30 kV 15 mA in the 10–80° 2 θ -range, with a scan speed of 0.25° min⁻¹ with a sampling width of 0.02°. The divergence slit was set at 1.25°, the receiving slit at 0.3 mm and the Anti-scattering slit at 1.25°. For the evaluation of the diffraction patterns Le Bail fitting was carried out with the program GSAS-II.^[36] A cosine function was used to model the amorphous background of the raw data. Based on the halide content of the samples the starting unit cell dimensions for the refinement were either $\text{Cs}_3\text{Cu}_2\text{Br}_5$ (COD #7246299) or $\text{Cs}_3\text{Cu}_2\text{I}_5$ (COD #7246300). Isotropic domain size and microstrain models were used to account for the peak broadening. X-ray photoelectron spectroscopy (XPS) measurements were performed with a SPECS instrument equipped with a PHOIBOS 150 MCD 9 hemispherical analyzer. The analyzer was in FAT mode with 40 eV pass energy for acquiring survey scans and 20 eV for high resolution scans. The Al $\text{K}\alpha$ radiation ($h\nu = 1486.6 \text{ eV}$) of a dual anode X-ray gun was used as an excitation source and operated at 150 W power. Ten scans were averaged to get a single high-resolution spectrum. The cesium 3d peak was used for charge referencing and set at 724.0 eV in all cases (reference measurement from CsI powder). For spectrum evaluation, CasaXPS commercial software package was used.^[37] Ultraviolet photoelectron spectroscopy (UPS) was performed with a He (I) excitation (21.22 eV) source. There was 10 V of external bias applied to the samples to accelerate secondary electrons to the analyzer. The recorded UPS spectra were corrected for additional He(I) lines. More details about the evaluation of the XPS, UPS spectra were provided in the Supporting Information.

Radioluminescence Measurements: The RL pulses from the thin-film samples were detected with a Hamamatsu (H1949-51) photomultiplier tube (PMT) connected to one hemisphere of a 50 mm diameter light integration sphere (THORLABS). The samples were exposed to α particles from an Am-241 source through an aperture of 1 mm. The distance between the source and the sample was 15 mm, which was taken into account in the calculation of the incident particle energy. The geometric layout of the apparatus was shown in Scheme S1 (Supporting Information). The light pulses generated by each α particle hitting the sample were converted to amplified electric pulses at the PMT anode, which inherited the time structure of the RL decay of the self-trapped excitonic states. This time structure was recorded by a waveform digitizer module with a sampling time of 2 ns. The total number of photons created in each α particle event could be deduced from the integration of the full pulse waveform, while the exponential time structure of the decay could be fitted and decomposed from the event-averaged waveforms.

Supporting Information

Supporting Information is available from the Wiley Online Library or from the author.

Acknowledgements

The authors thank O.D. and E.A.E. for the use and assistance in the steady state PL and PL lifetime measurements and D.U. and E.C. for the use and

the assistance in the PLQY measurements. This work was supported by the projects TKP2021-NKTA-42 and TKP-2021-NVA-19 financed by the National Research, Development and Innovation Fund of the Ministry for Innovation and Technology, Hungary. This work was further supported by the National Research, Development and Innovation Office (NKFIH) through the FK-138888 project and the University of Szeged Open Access Fund: 6397. G.F.S. also acknowledges the financial support of the János Bolyai Research Scholarship of the Hungarian Academy of Sciences.

Conflict of Interest

The authors declare no conflict of interest.

Data Availability Statement

The data that support the findings of this study are available from the corresponding author upon reasonable request.

Keywords

band structures, mixed-halides, radioluminescence, self-trapped excitons, trap states

Received: April 5, 2023
Revised: June 23, 2023
Published online: July 20, 2023

- [1] Z. Guo, J. Li, R. Pan, J. Cheng, R. Chen, T. He, *Nanoscale* **2020**, *12*, 15560.
- [2] Y. Li, Z. Zhou, N. Tewari, M. Ng, P. Geng, D. Chen, P. K. Ko, M. Qammar, L. Guo, J. E. Halpert, *Mater. Chem. Front.* **2021**, *5*, 4796.
- [3] Z. Ma, L. Wang, X. Ji, X. Chen, Z. Shi, *J. Phys. Chem. Lett.* **2020**, *11*, 5517.
- [4] Y. Nah, D. Solanki, D. H. Kim, *Cell Rep. Phys. Sci.* **2022**, *3*, 101171.
- [5] T. Jun, K. Sim, S. Iimura, M. Sasase, H. Kamioka, J. Kim, H. Hosono, *Adv. Mater.* **2018**, *30*, 1804547.
- [6] H. Chen, L. Zhu, C. Xue, P. Liu, X. Du, K. Wen, H. Zhang, L. Xu, C. Xiang, C. Lin, M. Qin, J. Zhang, T. Jiang, C. Yi, L. Cheng, C. Zhang, P. Yang, M. Niu, W. Xu, J. Lai, Y. Cao, J. Chang, H. Tian, Y. Jin, X. Lu, L. Jiang, N. Wang, W. Huang, J. Wang, *Nat. Commun.* **2021**, *12*, 1421.
- [7] S. Li, J. Luo, J. Liu, J. Tang, *J. Phys. Chem. Lett.* **2019**, *10*, 1999.
- [8] Y. Gu, X. Yao, H. Geng, G. Guan, M. Hu, M. Han, *ACS Appl. Mater. Interfaces* **2021**, *13*, 40798.
- [9] M. Zhang, J. Zhu, B. Yang, G. Niu, H. Wu, X. Zhao, L. Yin, T. Jin, X. Liang, J. Tang, *Nano Lett.* **2021**, *21*, 1392.
- [10] X. Ouyang, R. Lin, Y. Ding, Y. Liang, W. Zheng, L. Chen, X. Song, F. Huang, X. Ouyang, *Mater. Chem. Front.* **2021**, *5*, 4739.
- [11] L. Lian, M. Zheng, W. Zhang, L. Yin, X. Du, P. Zhang, X. Zhang, J. Gao, D. Zhang, L. Gao, G. Niu, H. Song, R. Chen, X. Lan, J. Tang, J. Zhang, *Adv. Sci.* **2020**, *7*, 2000195.
- [12] S. Cheng, A. Beitlerova, R. Kucerkova, M. Nikl, G. Ren, Y. Wu, *Phys. Status Solidi RRL* **2020**, *14*, 2000374.
- [13] X. He, Y. Deng, D. Ouyang, N. Zhang, J. Wang, A. A. Murthy, I. Spanopoulos, S. M. Islam, Q. Tu, G. Xing, Y. Li, V. P. Dravid, T. Zhai, *Chem. Rev.* **2023**, *123*, 1207.
- [14] M. Hunyadi, G. F. Samu, L. Csige, A. Csík, C. Buga, C. Janáky, *Adv. Funct. Mater.* **2022**, *32*, 2206645.
- [15] X. Li, J. Chen, D. Yang, X. Chen, D. Geng, L. Jiang, Y. Wu, C. Meng, H. Zeng, *Nat. Commun.* **2021**, *12*, 3879.
- [16] J. Feng, J. Wang, D. Wang, M. Han, G. Qian, F. Wu, Q. Lin, Z. Hu, *ACS Appl. Electron. Mater.* **2022**, *4*, 225.

- [17] X. Zhang, B. Zhou, X. Chen, W. W. Yu, *Inorg. Chem.* **2022**, *61*, 399.
- [18] X. Mo, T. Li, F. Huang, Z. Li, Y. Zhou, T. Lin, Y. Ouyang, X. Tao, C. Pan, *Nano Energy* **2021**, *81*, 105570.
- [19] H. Chen, J. M. Pina, F. Yuan, A. Johnston, D. Ma, B. Chen, Z. Li, A. Dumont, X. Li, Y. Liu, S. Hoogland, Z. Zajacz, Z. Lu, E. H. Sargent, *J. Phys. Chem. Lett.* **2020**, *11*, 4326.
- [20] M.-H. Du, *ACS Energy Lett.* **2020**, *5*, 464.
- [21] L. Lian, M. Zheng, P. Zhang, Z. Zheng, K. Du, W. Lei, J. Gao, G. Niu, D. Zhang, T. Zhai, S. Jin, J. Tang, X. Zhang, J. Zhang, *Chem. Mater.* **2020**, *32*, 3462.
- [22] C. Chen, Y. Lin, P. Lai, H. Lin, G. Tan, H. Lin, R. D. Schaller, *Adv. Opt. Mater.* **2022**, *10*, 2200005.
- [23] R. Lin, Q. Zhu, Q. Guo, Y. Zhu, W. Zheng, F. Huang, *J. Phys. Chem. C* **2020**, *124*, 20469.
- [24] R. Kentsch, M. Morgenroth, M. Scholz, K. Xu, J. Schmedt auf der Günne, T. Lenzer, K. Oum, *J. Phys. Chem. Lett.* **2020**, *11*, 4286.
- [25] Y.-K. Jung, S. Kim, Y. C. Kim, A. Walsh, *J. Phys. Chem. Lett.* **2021**, *12*, 8447.
- [26] P. Cheng, L. Sun, L. Feng, S. Yang, Y. Yang, D. Zheng, Y. Zhao, Y. Sang, R. Zhang, D. Wei, W. Deng, K. Han, *Angew. Chem.* **2019**, *131*, 16233.
- [27] R. Rocanova, A. Yangui, H. Nhalil, H. Shi, M.-H. Du, B. Saparov, *ACS Appl. Electron. Mater.* **2019**, *1*, 269.
- [28] D. P. McMeekin, G. Sadoughi, W. Rehman, G. E. Eperon, M. Saliba, M. T. Horantner, A. Haghighirad, N. Sakai, L. Korte, B. Rech, M. B. Johnston, L. M. Herz, H. J. Snaith, *Science* **2016**, *351*, 151.
- [29] Z. Jiang, H. Liu, J. Zou, Y. Huang, Z. Xu, D. Pustovyi, S. Vitusevich, *RSC Adv.* **2023**, *13*, 5993.
- [30] Y. Li, P. Vashishtha, Z. Zhou, Z. Li, S. B. Shivarudraiah, C. Ma, J. Liu, K. S. Wong, H. Su, J. E. Halpert, *Chem. Mater.* **2020**, *32*, 5515.
- [31] P. Sebastia-Luna, J. Navarro-Alapont, M. Sessolo, F. Palazon, H. J. Bolink, *Chem. Mater.* **2019**, *31*, 10205.
- [32] Z. Zhou, Y. Li, Z. Xing, H. H. Y. Sung, I. D. Williams, Z. Li, K. S. Wong, J. E. Halpert, *Adv. Mater. Interfaces* **2021**, *8*, 2101471.
- [33] D. Shen, X. Wang, X. Zhang, Y. Liu, Y. Shi, X. Li, X. Chen, Y. Zhang, *ACS Appl. Opt. Mater.* **2023**, *1*, 435.
- [34] G. K. Grandhi, N. S. M. Viswanath, H. Bin Cho, J. H. Han, S. M. Kim, S. Choi, W. Bin Im, *J. Phys. Chem. Lett.* **2020**, *11*, 7723.
- [35] M. Ng, P. Geng, S. B. Shivarudraiah, L. Guo, J. E. Halpert, *Adv. Opt. Mater.* **2022**, *10*, 2201031.
- [36] B. H. Toby, R. B. Von Dreele, *J. Appl. Crystallogr.* **2013**, *46*, 544.
- [37] N. Fairley, V. Fernandez, M. Richard-Plouet, C. Guillot-Deudon, J. Walton, E. Smith, D. Flahaut, M. Greiner, M. Biesinger, S. Tougaard, D. Morgan, J. Baltrusaitis, *Appl. Surf. Sci.* **2021**, *5*, 100112.